Wide-Field Calcium Imaging of Dynamic Cortical Networks During Locomotion

Sarah L. West[1, 2], Justin Aronson[1], Laurentiu S. Popa[1], Russell E. Carter[1], Aditya Shekhar[1], Kathryn D. Feller[1], Leila Ghanbari[3], Suhasa B. Kodandaramaiah[2,3,4], Timothy J. Ebner[1, 2]

[1]Department of Neuroscience, [2]Graduate Program in Neuroscience, [3]Department of Mechanical Engineering, [4]Department of Biomedical Engineering, University of Minnesota, Minneapolis, MN, USA.

Abbreviated Title: Wide-field Calcium Imaging During Locomotion

Correspondence: Timothy J. Ebner, M.D., Ph.D.
Department of Neuroscience
University of Minnesota
Lions Research Building, Room 421
2001 Sixth Street S.E.
Minneapolis, MN 55455
Phone: 612-626-9204
Fax: 612-626-9201
Email: ebner001@umn.edu

Number of Pages: 35
Number of Figures: 9
Number of words: Abstract (242), Significance Statement (118), Introduction (649), and Discussion (1458)
Conflict of Interest Statement: The authors declare no competing financial interests.

Acknowledgements:
We would like to thank Lijuan Zhuo, William Chiesl, and Morgan Gerhart for their assistance in animal surgeries and data collection. This work was partially supported by National Institutes Health grants NS111028 (to S.B.K. and T.J. E.), R61/R33 NS115089 (to T.J.E.), and T32-MH115688 (to S.L.W.).

ABSTRACT

Behavior results in widespread activation of the cerebral cortex. To fully understanding the cerebral cortex's role in behavior therefore requires a mesoscopic level description of the cortical regions engaged and their functional interactions. Mesoscopic imaging of Ca^{2+} fluorescence through transparent polymer skulls implanted on transgenic Thy1-GCaMP6f mice reveals widespread activation of the cerebral cortex during locomotion, including not just primary motor and somatosensory regions but also premotor, auditory, retrosplenial, and visual cortices. To understand these patterns of activation, we used spatial Independent Component Analysis (sICA) that segmented the dorsal cortex of individual mice into 20-22 Independent Components (ICs). The resulting ICs are highly consistent across imaging sessions and animals. Using the time series of Ca^{2+} fluorescence in each IC, we examined the changes in functional connectivity from rest to locomotion. Compared to rest, functional connectivity increases prior to and at the onset of locomotion. During continued walking, a global decrease in functional connectivity develops compared to rest that uncovers a distinct, sparser network in which ICs in secondary motor areas increase their correlations with more posterior ICs in somatosensory, motor, visual, and retrosplenial cortices. Eigenvector centrality analysis demonstrates that ICs located in premotor areas increase their influence on the network during locomotion while ICs in other regions, including somatosensory and primary motor, decrease in importance. We observed sequential changes in functional connectivity across transitions between rest and locomotion, with premotor areas playing an important role in coordination of computations across cortical brain regions.

SIGNIFICANCE

Behavior such as locomotion requires the coordination of multiple cerebral cortical regions to accurately navigate the external environment. However, it is unclear how computations from various regions are integrated to produce a single, coherent behavioral output. Here, wide-field, epifluorescence Ca^{2+} imaging across the dorsal cerebral cortex reveals the changing functional interactions among cortical regions during the transition from rest to locomotion. While functional connectivity among most cortical nodes primarily decreases from rest to locomotion, a well-defined network of increased correlations emerges between premotor and other cortical regions with an increase in the importance of the premotor cortex to the network. The results suggest that the role of the premotor areas in locomotion involves coordinating interactions among different cortical regions.

INTRODUCTION

Behavior involves processing and integrating information within and across multiple brain regions. However, the mechanisms by which neuronal activity is coordinated across the cerebral cortex to produce a unitary behavioral output are not well understood. A prominent view is that sensory, motor, and cognitive behaviors emerge from the neuronal interactions in and among regions (Harris, 2005; Buzsaki, 2010; Carrillo-Reid et al., 2016; Allen et al., 2017; Musall et al., 2019). This view implies that the operation of the brain cannot be easily understood by studying its components in isolation. Even simple sensory stimuli and motor tasks involve multiple cortical areas. For example, deflection of a single whisker results in activation across the sensorimotor cortices (Ferezou et al., 2007). Discrete, uninstructed movements dominate neural activity in premotor, motor, somatosensory, and visual cortices (Musall et al., 2019). Arousal and attention exert markedly different spatial and temporal effects on cortical activity (Harris and Thiele, 2011; McGinley et al., 2015b; Shimaoka et al., 2018). Furthermore, motor learning produces widespread changes in cortical dynamics (Makino et al., 2017). Single unit recordings have demonstrated that locomotion modulates neuronal activity in many cerebral cortex regions (Saleem et al., 2013; Lee et al., 2014; Schneider et al., 2014; Dipoppa et al., 2018). The complexity of cortical activation dynamics, therefore, necessitates a mesoscopic level description of the activity and the interactions among regions to understand cerebral cortical function during behavior. Here, we examine the interactions among different cortical areas during the transition from rest to walk using mesoscopic Ca^{2+} imaging.

While the mesencephalic locomotor region can initiate locomotion and the spinal cord central pattern generators produce the characteristic rhythmic patterns of muscle contractions (Josset et al., 2018; Sharma et al., 2019), the cerebral cortex provides important contributions to walking. The primary (M1) and premotor cortices, as well as the posterior parietal cortex (PPC), are important for accurate limb placement (Drew and Marigold, 2015). Lesioning the corticospinal tract or M1 produces locomotor deficits, including hypermetria and abnormalities in limb trajectory and intralimb coordination (Liddell and Phillips, 1944). Pyramidal neuronal firing in M1 correlates with individual muscle activity during locomotion (Drew et al., 2008a; Drew et al., 2008b; Drew and Marigold, 2015) and modulates when the subject maneuvers around an obstacle, suggesting M1 directly controls locomotion and influences the central motor pattern. The PPC is highly engaged in planning aspects of locomotion, as it contributes to obstacle navigation by creating an appropriate motor plan that includes integrating visual, somatosensory, vestibular, and auditory information (Drew and Marigold, 2015; Takakusaki, 2017).

Locomotion also engages many cortical regions that are not explicitly involved in controlling the motor pattern. Primary somatosensory neurons respond in phase to locomotor rhythms (Chapin and Woodward, 1982) and modulate their discharge both before and after gait adjustments (Favorov et al., 2015). Neurons in the primary

visual cortex (V1) are highly modulated by locomotion, including increased firing rates, enhanced gain and improved encoding and stimulus discrimination (Niell and Stryker, 2010; Dadarlat and Stryker, 2017). In addition, locomotion alters neural activity in the primary auditory cortex, reducing gain by increasing the activity of inhibitory interneurons (Schneider et al., 2014; Zhou et al., 2014; McGinley et al., 2015a; Schneider and Mooney, 2018). Wide-field Ca^{2+} imaging during locomotion also demonstrates increased interactions between V1 and the retrosplenial area (Clancy et al., 2019).

In this study we examine the functional interactions occurring across the dorsal cerebral cortex in head-fixed mice during locomotion as compared to awake quiescence (rest). Mesoscopic Ca^{2+} imaging reveals large increases in fluorescence across the dorsal cerebral cortex, both before and during locomotion. Spatial Independent Component Analysis (sICA) identified a highly reproducible set of functionally independent cortical regions (i.e., Independent Components (ICs)). During locomotion, a unique pattern of functional connectivity develops among these ICs, with those in anterior premotor regions playing a larger role in that network. This work provides a new understanding of cortical processes and functional connectivity during locomotion.

MATERIALS AND METHODS

All animal studies were approved by and conducted in conformity with the Institutional Animal Care and Use Committee of the University of Minnesota.

Animals and surgical procedures

Eight (5 male, 3 female) transgenic C57BL/6J, Thy1-GCaMP6f (Jackson laboratories JAX 024339) mice expressing GCaMP6f in excitatory pyramidal neurons of the cerebral cortex were used (Dana et al., 2014). To obtain optical access to a large region of the dorsal cerebral cortex, we implanted morphologically conformant windows made from transparent polymer (Ghanbari et al., 2019). Prior to surgery, animals were administered slow release buprenorphine and then anesthetized with isoflurane (5% induction, 0.5-3% maintenance). The head was shaved and mounted in a stereotaxic frame that did not damage the auditory meatus. Depth of anesthesia was monitored by toe pinch response every 15 min. Isoflurane levels were adjusted with an increase in heart rate or if a response to pain was registered. Body temperature was maintained constant (37˚C) using a feedback-controlled heating pad and the corneas were protected with eye ointment. The surgical procedure began with excision of the scalp followed by removal of the facia so that the positions of lambda and bregma could be recorded. High resolution images with a reference scale were captured both before and after securing the implant to the skull using a digital microscope camera (S01-0801A, Science Supply) attached to the surgical microscope to allow for identification of bregma after removing the skull. A manual craniotomy removed a flap of skull that matched the

geometry of the implant window, leaving the dura intact. The implant was aligned to the craniotomy and fixed to the skull using a bone screw (F000CE094, Morris Precision Screws and Parts) placed 2-3 mm posterior to lambda. The implant periphery was glued to the skull (Vetbond, 3M) and cemented in place with dental cement (S380 S&B Metabond, Parkell Inc.). Following the cure of the cement, a custom, head-fixing titanium frame was fastened to the implant using three screws (3/32" flat head 0-80). A second application of dental cement enclosed the fastening screws. After surgery the mice recovered on a heating pad to ambulatory state and then were returned to a clean home cage. Mice were administered meloxicam (2 mg/kg, s.c.) for three days and allowed a minimum of seven days to recover before any experimental procedures were initiated.

Behavioral setup

Mice were housed in a reversed light-dark (12h-12h) room with experiments performed during the dark period, which is the normal waking and high activity phase of the circadian cycle in mice. After recovery from surgery, polymer window-implanted mice were habituated to the behavioral setup in increasing time increments (5 min, 15 min, 40 min, 1 hr) before experiments. For the behavioral setup, the mouse was head-fixed on a low-friction, horizontal disk treadmill that allowed for natural movements such as walking and grooming. Once habituated, animals alternated between periods of awake quiescence (i.e., rest) and spontaneous walking, which were used for spontaneous locomotion analysis. To offset any potential effects created by the mildly curved path of the disk treadmill, a subset (22 of 62) of experimental sessions were recorded with the mouse head-fixed to the disk pointing in the opposite direction.

Locomotion kinematics were calculated from the treadmill angular displacement as measured by a high-resolution rotary encoder and recorded by an Arduino microcontroller (Arduino Uno, www.arduino.cc) at 1 kHz. Velocity was determined and smoothed using a sliding average (100 bins, 1 bin step size). Locomotion was defined as periods of movement in which the wheel reached a velocity of 0.25 cm/s or greater. Working back from 0.25 cm/s, movement onset was then defined as the time wheel velocity first exceeded 0 cm/s, and offset was defined as the time velocity returned to 0 cm/s. Periods in which velocity remained between -0.25 cm/s and 0.05 cm/s were labeled as rest, while all remaining periods were discarded as "fidgeting" or backwards walking.

Fluorescence imaging and behavioral recording

Head-fixed mice were placed on the treadmill beneath a Nikon AZ-100 microscope. Single-photon fluorescence imaging was performed using a high-speed, Electron Multiplying CCD (Andor, iXon3) controlled with MetaMorph (Molecular Devices Inc.). Using the variable magnification function, the field-of-view was optimized to image the exposed dorsal cortical surface (6.2 mm x 6.2 mm) with a spatial resolution of 256 x 256 pixels (pixel size of ~41 μm x 41 μm). Images were acquired at 20 Hz for 5 mins (6000 frames), and 12 imaging trials

were obtained in a session (i.e., all trials obtained in 1 day). Time between imaging trials ranged between 1-5 mins.

Two high-speed, IR-sensitive CMOS cameras (DMK 33UP1300, The Imaging Source, or Flea3, Point Grey) recorded the behavior at 40 Hz throughout a session, under diffuse infrared light that did not interfere with the Ca^{2+} imaging. Behavioral videos were recorded using Spinnaker SDK software (FLIR Systems).

Fluorescence imaging analysis

Epifluorescence imaging data were processed in non-overlapping segments of 1 min irrespective of the animal's behavior. Pre-whitened data was decomposed into principal components. Out of 1200 components, the first 24 that explained more than 99% of variance were retained. We computed the 24 corresponding spatial ICs using the Joint Approximation Diagonalization of Eigenmatrices (JADE) algorithm that decomposes mixed signals into ICs by minimizing the mutual information with a series of Givens rotations (Cardoso, 1999; Makino et al., 2017; Sahonero-Alvarez and Calderon, 2017). This method provides a blind segmentation of the cerebral cortex based only on statistical properties of the Ca^{2+} activity and does not use any prior assumptions regarding cerebral function or architecture. The ICs were z-scored and thresholded so that values below 1.5 were set to zero. For each IC, all domains formed by contiguous pixels were registered. Domains covering less than 500 pixels were discarded as physiologically irrelevant. An IC that included multiple discontinuous domains, for example homotopic cortical regions, was separated into multiple ICs including only single domains. Further, upon visual inspection we eliminated artifact ICs that were not associated with cortical activity including vascular artifacts.

For each recording day, ICs were grouped into spatially distinct clusters. To generate these IC clusters, the spatial correlations (σ) of the z-score maps between all ICs from a recording day were calculated. A hierarchical clustering method was used to identify significantly different clusters (Kimes et al., 2017). Ward's distance was used to cluster ICs into potential clusters of size 1 up to a single cluster that contained all the ICs. As the potential number of clusters decreased, each new joining of clusters was determined to be statistically significant or not. All ICs included in a division were randomly shuffled between the two new clusters, and the mean spatial correlation between ICs in one group was calculated and divided by the mean correlation between all the ICs in the cluster. This shuffling was repeated 1000 times for each division to create a null distribution of correlation ratios. Only divisions with a correlation ratio in the highest 95% of the distribution ($\alpha = 0.05$) were considered significant. For analysis, the ICs were grouped into the maximum number of significant clusters. Spatial correlation measures tended to divide ICs with high spatial overlap into separate clusters. To avoid these artificial divisions, clusters had to contain 20 or more ICs and have a Ward's distance greater than 10 to be included. The z-score maps of

ICs within each significant cluster were averaged together to create a prototypical IC for that cluster. Visual identification of IC clusters corresponding to artifacts or blood vessels were manually identified and excluded.

To compare the occurrence and shape of the IC clusters across recording days, image frames were spatially registered using affine transformations. We utilized a built-in MATLAB (Mathworks) function (imregtform, with the OnePlusOneEvolutionary optimizer and the MeanSquares optimization) to register frames from an imaging session to frames from a representative session. All sessions were registered to the same representative session for a mouse.

A manual method of IC identity assignment was used to generate a catalog representative of all clusters across days in each mouse. IC clusters from each recording session were visually compared across days and manually assigned identities to create a catalog of ICs that represented all the IC clusters in a mouse. Similar to how the daily IC clusters were created, the maps of all IC clusters with a given catalog identity were averaged together to create the catalog IC for each mouse. Masks were created by thresholding values greater than 0.3 times the maximum z score value in that catalog IC. The mean spatial correlation of the IC clusters within each catalog IC is high ($\sigma > 0.8$, Fig 3E), demonstrating the consistency of the cataloged ICs over time.

Functional connectivity analysis

The masks from the IC catalog for each mouse were used to extract mean fluorescence time series for functional connectivity analysis, and the resulting time series were linearly detrended. Recordings were divided into 6 behavioral periods each 3s in duration, as defined by treadmill velocity (see Fig. 4A): 1) rest (see definition above); 2) pre-locomotion (rest just prior to locomotion onset; "pre."); 3) locomotion initiation (locomotion just after locomotion onset; "init."); 4) continued locomotion (periods of locomotion outside of transition periods; "cont'd"); 5) termination of locomotion (locomotion just prior to locomotion offset; "term."); and 6) post-locomotion (rest just after locomotion offset; "post."). Periods of rest or continued locomotion that lasted longer than 3s were divided into multiple 3s segments, and data at the end of the period was removed. Periods less than 3s were also removed. We chose 3s periods (60 time points) because this provides sufficient data to calculate robust Pearson correlations on the associated fluorescence time series for the functional connectivity analysis.

For each 3s period, the correlation coefficients (ρ) were calculated between the time series from all IC to generate a correlation (i.e., adjacency) matrix, and these matrices were averaged to create mean adjacency matrices for each behavior period. Within each experimental animal, significant change in correlations of two ICs between behavior periods were calculated using custom MATLAB code. For each IC pair, the correlations from each behavior period were compared to those from the other behavior periods with a t-statistic. This t-statistic was then

compared to a null distribution of t-statistics from correlations from 500 reshufflings of the correlations across behavior. Significance was determined by $\alpha<0.05$ with Bonferroni correction.

To further quantify the functional relationships between brain regions during locomotion, the network centrality of ICs was calculated on 3s correlation matrices using MATLAB code from the Brain Connectivity Toolbox (Rubinov and Sporns, 2010). The eigenvector centrality was calculated for the catalog ICs using the correlation matrices from each 3s period, and these centralities were compared across behavior periods with a t-statistic. Similar to the comparisons among the correlations between ICs, this t-statistic was compared to a null distribution of t-statistics from 500 reshufflings of the centralities across behavior. Again, significance was determined by $\alpha<0.05$ with Bonferroni correction.

To group data across animals, ICs in each mouse catalog were assigned to one of 18 regions of interest (9 per hemisphere) that were present across all mice (Fig. 5A). Correlation values between ICs in the catalog were reassigned to these new regions. If more than one catalog IC was assigned to a region, then the correlation values for that region were taken as the mean correlations of those catalog ICs. To calculate significant changes in correlation across behavior periods, correlations were normalized across mice by removing the mean correlation for each animal and combined with other animals as z-scores. Significant changes in correlations between regions, region centrality scores, and significant changes in centrality scores were calculated as described above and reported as s.d. from the normalized mean.

Hemodynamic correction

Blood flow increases with neuronal activation, and oxygenated blood absorbs light with peak absorption at ~530 nm, decreasing the duration of the increased GCaMP fluorescence (Ma et al., 2016). Therefore, additional experiments were performed to evaluate the effects of hemodynamics and other Ca^{2+} independent fluorescence changes such as flavoprotein autofluorescence (Vanni and Murphy, 2014; Jacobs et al., 2018), using 4 mice (1 from the original cohort and 3 additional). We used dual-wavelength illumination to capture both Ca^{2+}- dependent (470 nm, blue light) and Ca^{2+}- independent (405 nm, violet light) GCaMP6f signals on consecutive frames using a Cairn OptoLED driver (Cairn OptoLED, P1110/002/000; P1105/405/LED, P1105/470/LED) (Ma et al., 2016; Allen et al., 2017; Jacobs et al., 2018; Musall et al., 2019; MacDowell and Buschman, 2020). An excitation filter (ET480/40, Chroma) was placed in front of the 470 nm LED, then both light sources were combined into the parallel light path of a Nikon AZ100M macroscope through a dichroic mirror (425 nm, Chroma T425lpxr), and then reflected off a second dichroic (505 nm, Chroma T505pxl) to the brain. Cortical GCaMP6f emissions then passed back through a second dichroic into a sCMOS camera (Andor Zyla 4.2 Oxford Instruments). Exposure times for each frame was 18ms, synced via TTL pulses from a Cambridge Electronics 1401 (Cambridge

Electronic Design Limited) acquisition system that controlled both LEDs and the external trigger of the Andor Zyla 4.2. Frames were captured at 40 Hz (20 Hz per channel) at 256x256 pixels per image.

Using a previously described correction method (Ma et al., 2016; Jacobs et al., 2018; MacDowell and Buschman, 2020), the Ca^{2+}-independent signals were removed by first calculating the per-pixel average intensity in both channels, then scaling the 405 nm channel to a similar level of the 470 nm channel by multiplying by the ratio of the per-pixel averages. The scaled 405 nm signal was then subtracted from the 470 nm signal and the resulting signal was then normalized by dividing by the scaled 405 nm signal. All subsequent processing, including sICA, functional connectivity and network measures, was identical to that preformed on the 470 nm images.

All MATLAB analysis code for sICA segmentation of mesoscale Ca^{2+} imaging; eigenvector centrality; and hemodynamic correction are available upon request**.**

RESULTS

Database

The main results are based on imaging data collected from eight GCaMP6f transgenic mice. Eight imaging sessions were performed on seven of the animals, while six imaging sessions were performed on the remaining animal, resulting in a total of 62 sessions. During each imaging session, we obtained 60 min of data (12 trials x 5 min each), resulting in 480 min of imaging in 7 animals and 360 min in 1 mouse. Mice spent an average of 75.7 ± 10.5% of recording time at rest, 21.3 ± 10.4% locomoting, 2.2 ± 0.9% fidgeting, and 0.9 ± 0.4% of recording time moving backwards. Across the 8 mice, we fully analyzed a total of 2,743 min of awake quiescence and 776 min of spontaneous locomotion.

Changes in Ca^{2+} epifluorescence during behavior

Mice were head-fixed over a disk treadmill that allowed for spontaneous locomotion (Fig. 1A) and wide-field Ca^{2+} imaged through an implanted polymer skull (Ghanbari et al., 2019) (Fig. 1B). In agreement with previous reports, wide-field Ca^{2+} imaging reveals widespread activation across the dorsal cerebral cortex during both spontaneous locomotion (Fig. 1C top) and awake quiescence (Fig. 1C bottom). For each animal, spontaneous locomotion is characterized by an alternating and rhythmic step cycle typical of coordinated walking movement (Fig. 1D-F). During locomotion, Ca^{2+} fluorescence increases in motor regions, primary sensory areas (including somatosensory and visual cortices) and throughout posterior parietal and retrosplenial areas. Across these regions in all mice, the increases in fluorescence begin 880 ± 96 ms before the onset of locomotion by an increase greater than the mean + 2.5 s.d of the fluorescence at rest. These patterns of complex, temporal-spatial activity agree with

previous reports of motor, somatosensory, parietal, auditory, retrosplenial and visual cortical engagement during locomotion (Drew et al., 2008b; Niell and Stryker, 2010; Petersen et al., 2012; Saleem et al., 2013; Favorov et al., 2015; Drew and Marigold, 2015; Schneider and Mooney, 2018; Clancy et al., 2019) and highlight the involvement of multiple cerebral cortical regions in processing and integrating information related to locomotion.

Functional segmentation of the cortex reveals consistency across time and behavior

We segmented cortical activity into functionally distinct regions based on changes in Ca^{2+} fluorescence using sICA, a blind source separation tool commonly used in fMRI studies (Cardoso, 1999; Makino et al., 2017; Sahonero-Alvarez and Calderon, 2017). By minimizing the mutual information between regions to segment the cortex, sICA does not make assumptions about the underlying neuroanatomy of individual animals.

Taking advantage of our large imaging database, we initially evaluated the stability and repeatability of the ICs obtained from three levels of data: single day ("session"); across sessions; and across mice. For each 1 min epoch in a single session, the behavior-independent, sICA yield 10-20 ICs (z-score maps of 10 example ICs in Fig. 2A). The ICs occur in the same spatial region between epochs, so we used hierarchical clustering to identify consistent ICs. Ward's method of hierarchical agglomerative clustering identified significant clusters of ICs ("IC clusters") for all 1-min epochs in a session (Fig. 2B and C). For example, in a single session of a single mouse, 19 IC clusters were identified, and the individual ICs have a high probability of occurring in each 1 min epoch (Fig. 2B). Across all mice, the spatial correlation (σ) for the ICs obtained in each 1 min epoch averaged 0.55 ± 0.06 (mean ± s.d.), highlighting the consistency of ICs obtained within a 1-hour recording session. When superimposed on the brain, the ICs cover most of the imaged cortical area (Fig. 2C).

Next, we compared IC clusters over recording sessions. Six or eight recording sessions were obtained from each animal over a three-month period (five animals) or a six-month period (three animals). We found similar IC clusters within a mouse, regardless of the range of the time period (Fig. 3A), and individual ICs have a high probability of occurrence in each session (Fig. 3C). A catalog of ICs ("IC catalog") was generated across sessions for each mouse (Fig. 3B and D). For each mouse, σ is remarkably high across each recording sessions of the ICs in each catalog (0.85 ± 0.032), demonstrating the robust spatial correspondence in the cortical segmentation obtained with sICA (Fig. 3E). Though there are considerable similarities in the IC catalogs across all 8 mice, some individual differences are observed. We tested the impact of these differences by evaluating the functional connectivity between rest and locomotion in each individual mouse IC catalog as well as in pooled data from all mice.

Functional connectivity during behavioral transitions

To analyze the functional connectivity of the cortex during the transitions between rest and locomotion, we extracted the average of the fluorescence time series from each IC (Fig. 4). At the transitions from rest to walking, all ICs exhibit an increase in activity prior to locomotion that peaks around the onset of locomotion (Fig. 4A). Throughout locomotion, neural activity remains elevated compared to rest and, on return to rest, fluorescence levels decrease to baseline levels (Fig. 4A). This pattern of fluorescence changes within the ICs agrees with the wide-field activity observed across the entire cortex (see Fig. 1C) and was present in all mice.

To understand the functional coupling among the ICs during these transitions, we divided each locomotion time course into six behavioral periods, each 3s in length: 1) rest, 2) pre-locomotion, 3) initiation of locomotion, 4) continued locomotion, 5) locomotion prior to termination, and 6) rest after termination of locomotion (see Methods and Fig. 4A). Within each 3s behavioral period for a mouse, the Pearson correlation (ρ) was calculated between time series for each possible pair of ICs. The resulting correlation coefficients were then averaged across all instances of the behavior period in that mouse. The average correlation coefficients between ICs were plotted as both correlation matrices (Fig. 4B) and network graphs (Fig. 4C). Each node of the network graph represents the corresponding IC and is placed at the center of mass of the composite z-score map. These results reveal high average correlation coefficients between most ICs.

In the 3s period prior to the onset of locomotion ("pre.") the correlation matrices reveal a sharp, increase in the correlation between all ICs ($F(5,804) = 102$, $p = <2e\text{-}16$, ANOVA; $p = <1e\text{-}6$, TukeyHSD [Honest Significant Difference] test; Fig. 4B). These correlation values then gradually decrease over time as the animal enters the initiation of locomotion period ($p = 1.140e\text{-}4$, TukeyHSD) and proceeds into continued locomotion ($p = <2e\text{-}16$, TukeyHSD; Fig. 4B). Correspondingly, the network graphs become highly connected before locomotion onset. These connections are maintained during locomotion initiation and become more sparsely connected as locomotion continues, as shown in the corresponding treadmill velocity traces (Fig. 4C). For the transition back to rest, the network once again becomes highly correlated ($p = <2e\text{-}16$, TukeyHSD).

To compare results across mice as well as with previous studies, we identified 18 ICs (9 per hemisphere) common to all mouse catalogs (Fig 5A-B). These ICs were mapped onto the Common Coordinate Framework and are located near motor, somatosensory, parietal, visual, and retrosplenial areas. The correlation patterns observed in individual mice (Fig 4) also hold true using these population data (Fig. 5). The correlation matrices and network graphs averaged across all 8 experimental animals show significant increases in correlations and connectivity across the cortical network ($F(5,42) = 20.68$, $p = 2.3e\text{-}10$, ANOVA) prior to and after the onset of locomotion ($p = 0.0089$, TukeyHSD), decreases during continued locomotion ($p = 0.0017$, TukeyHSD) and an increase in

functional connectivity on return to rest ($p = 9.1e-6$, TukeyHSD). At group level, locomotion is associated with a global increase in cortical connectivity, both preceding and following the behavior. Interestingly, continued walking engages a more sparsely connected network, with ICs within M2 and the retrosplenial cortex among the most highly connected regions.

A t-test with permutations and Bonferroni correction was used to evaluate the significant changes in mean correlations between behavior periods (Fig. 6A). Compared to rest, all pre-locomotion correlations between ICs increased significantly (231 of 231 possible connections increase with 0 significant decreases; $\alpha < 0.05$ with Bonferroni correction Fig. 6B). During continued locomotion compared to rest, however, there is a significant decrease in correlations between most ICs, particularly ICs located in motor, somatosensory, posterior parietal, and visual regions (Fig 6B, 165 of 231 possible connections). Notably, these functional connectivity increases primarily involve the two ICs aligned with the secondary motor region, M2. Of the 26 connections with a significant increase, 22 involve these anterior ICs, and these increased correlations include bilateral targets. Three of the remaining four increased correlations occur between ICs corresponding to primary motor regions. Correlations increase again during the termination of locomotion (86 of 231 possible connections increase with 0 decreases).

An identical pattern of increases and decreases in functional connectivity were observed in all mice. During pre-locomotion compared to rest, correlations increase significantly between most ICs (150 of 153 possible connections) and then decrease during continued locomotion (96 of 153 connections, Fig. 6C). As for the example mouse, there are increases in correlation between the most anterior ICs in M2 (ICs 1 and 2 in Fig. 5A) and nearly all other regions from rest to continued locomotion across mice (including 22 of 33 possible connections from these anterior ICs). Furthermore, there are significant increases in correlation between ICs in other motor regions (8 of the 12 remaining increases involve ICs 3-6 in Fig. 5A). Remarkably, connectivity does not increase between homotopic ICs. During the transition to post-locomotion, correlations between ICs increase to baseline rest levels (83 of 153 connections increase and 2 decrease). These observations show that relative to rest, continued locomotion involves select increases in functional connectivity, dominated by interactions with ICs in the secondary motor cortex.

To further characterize these changes in network structure, we calculated the mean eigenvector centrality of ICs within each behavior period and compared how the centrality changed between periods. Eigenvector centrality provides a measure of how tightly connected the behavior of a node is connected to all other nodes in the network (Rubinov and Sporns, 2010). Significant changes in eigenvector centrality occur from rest to continued locomotion for many ICs, as shown for two mice in Figure 7. The most prominent changes include a significant

increase in centrality from rest to continued locomotion for ICs located in M2 and, conversely, a decrease in centrality for other ICs, including those in the somatosensory, posterior parietal, and visual areas (Fig. 7A and B). Similarly, grouped data show the same pattern of changes in eigenvector centrality from rest to continued locomotion (Fig. 8A), supporting the concept that secondary motor regions increase their network importance in cortical processing during locomotion by communicating with all other regions of the dorsal cerebral cortex.

Comparing the significant changes in centrality scores across the transitions of adjacent behavior periods (Fig. 8B), reveals the progressive changes in network importance for the different regions. For ICs within M1, increases in centrality occur prior to locomotion onset, preceding the increases in centrality of ICs in M2, which occurs at locomotion onset. The ICs in M1 decrease in centrality once continued locomotion is reached, while the centrality of ICs in M2 remains elevated until locomotion offset. The centrality of ICs in M1 again increases before locomotion offset and then returns to baseline after offset. For ICs in retrosplenial regions, the largest increases in centrality occur between initiation to continuation of locomotion and between post-locomotion and rest. These changes in centrality and network importance highlight the dynamic roles played by functional regions and their interactions between behavior periods.

Hemodynamics contributions

We imaged 4 mice using dual-wavelength imaging to correct for Ca^{2+}- independent changes in fluorescence to remove the hemodynamic component from the GCaMP signal. The first step compared the catalogs generated for the four animals. As shown in the example mouse, the two catalogs were very similar including location and shape with the exception that not all ICs were present in the corrected catalog (Fig. 9A). At the population level, the spatial correlation between the ICs across imaging sessions was 0.91± 0.046. Similar patterns of changes in correlation were seen as in the not-corrected data (see Fig. 5C). The change in the patterns of connectivity for the corrected data from rest to continued walking (Fig. 9C) decreases between most ICs, but a cortical network develops in which ICs located in secondary motor areas increase their correlations with more posterior ICs. On termination of locomotion, functional connectivity returns to the rest state. Similarly, eigenvector centrality shows that ICs in these premotor regions increase their network importance during locomotion and many other IC decrease in importance (Fig. 9D). These data demonstrate that the blood flood have minimal effects on our sICA segmentation and network connectivity during the transitions between rest and locomotion.

DISCUSSION

Three key findings resulted from this wide-field Ca^{2+} imaging study of the mouse cerebral cortex during locomotion. First, sICA segmentation of the dorsal cortex results in highly reproducible ICs across time and

individual mice, both with and without hemodynamic correction. Second. robust and reproducible patterns of functional connectivity emerge between ICs that occur at discrete times in the transition from rest to locomotion and the return to rest. The cortical network during continued locomotion is characterized by increased correlations between secondary motor areas with more posterior ICs. Third, the sequence of changes that occur in premotor regions, as measured by eigenvector centrality, increase their network importance during locomotion, while other ICs decrease in importance.

Cortical segmentation with sICA

In the present study, sICA uncovered 18-22 independent spatial regions per mouse that we used to characterize the changes in Ca^{2+} epifluorescence. A previous implementation of sICA using JADE (Makino et al., 2017) obtained 16 ICs of approximately similar size and locations across the dorsal cerebral cortex. Our somewhat greater number of ICs can likely be attributed to imaging through transparent polymer windows as opposed to thinned bone as well as differences in the data collection, filtering and analyses. Extending those earlier findings, we show that the same ICs occur across weeks and even months, as well as similar, although not identical, ICs across mice. The ICs cover the imaging field, as required of a strong segmentation method (Rubinov and Sporns, 2010). The robustness of the ICs argues strongly for their functional relevance, as various ICA analyses have been extensively vetted and used to determine patterns of spatial activation in MRI and EEG studies (Godschalk et al., 1985; McKeown et al., 2003; Calhoun and de, 2017). Spatial ICA has been instrumental in establishing and probing brain normal and disordered networks in humans, such as default, sensory-motor and salience networks (Raichle et al., 2001; Greicius et al., 2003; Greicius et al., 2009; Dipasquale et al., 2015).

The ICs do not match the cortical segmentation defined by the Common Coordinate Framework (Allen Institute for Brain Science, 2015), suggesting that the minimization of mutual information between regions by sICA provides a complementary approach to that provided by the Common Coordinate Framework. Here we elected to determine the ICs independently and then align the ICs with the major cortical divisions in the mouse. Our implementation of sICA was performed over a 1 min window that allowed for determination of the ICs over many data points (1200 images). Other segmentation approaches used with wide-field Ca^{2+} imaging include seed-based correlation (Vanni et al., 2017), seed-correlation co-localized with tract-tracing (Mohajerani et al., 2013), spike-triggered mapping (Xiao et al., 2017), and non-negative matrix factorization (MacDowell and Buschman, 2020). While there have been few direct comparisons of these methods in Ca^{2+} imaging, different analytical approaches will likely provide complementary information.

While we did not normalize for changes in blood flow in the original 8 mice used in these experiments, sICA mitigates some of the contribution, including removal of blood vessels (Ma et al., 2016). In a group of 4 animals,

we determined the influence of increased blood flow on the spatial ICs and the functional connectivity network, using dual wavelength imaging (470 and 405 nm) to remove Ca^{2+}-independent changes. Removing the Ca^{2+}-independent signal produced IC catalogs similar to those catalogs produced from the uncorrected signal. Furthermore, the functional connectivity analyses on corrected signals revealed connectivity changes across behavior periods similar to those found with uncorrected signals. Therefore, the additional dual wavelength experiments agree with previous reports that the hemodynamic contribution to GCaMP6 Ca^{2+} response is limited (Vanni and Murphy, 2014; Makino et al., 2017; Allen et al., 2017; Jacobs et al., 2018; Musall et al., 2019).

Functional connectivity during the transitions from rest to locomotion

Our findings confirm previous studies demonstrating that locomotion activates many regions in the cerebral cortex (Niell and Stryker, 2010; Ghose, 2015; Dadarlat and Stryker, 2017). Using the IC catalogs, we observed a common pattern of changes in functional coupling among the ICs from rest to locomotion and on return to rest. When compared to rest, there are widespread increases in functional connectivity prior to and during initial locomotion. Relative to rest, continued locomotion is characterized by a new pattern of connectivity with two distinct features. The first is a large decrease in cortical connectivity across the hemispheres. The second is ICs within the premotor area increase their functional connectivity with more posterior ICs, specifically with ICs located in somatosensory, posterior parietal, visual, and retrosplenial cortices, regions known to be engaged during locomotion (Marigold et al., 2011; Saleem et al., 2013; Favorov et al., 2015; Alexander and Nitz, 2015; Clancy et al., 2019). Functional connectivity increases between anterior and posterior ICs bilaterally. The ICs located in M2 of this "locomotor network" have large increases in eigenvector centrality relative to rest. The ICs in barrel fields and retrosplenial regions have smaller but significant increases in centrality, while ICs in primary motor cortices decreased in network importance. Therefore, the cerebral cortex's role in sustained locomotion is defined by a specific network. Just prior to and after stopping locomotion, many of these changes revert with a decrease in importance of the ICs in M2 and the retrosplenial region and increases in other ICs. This intriguing pattern of cortical connectivity during sustained locomotion is suggestive of a functional network for locomotion.

While much of neural locomotor activity is determined by subcortical and spinal cord circuitry (Sharma et al., 2019), Drew and colleagues emphasized that the role of the M1 and PPC in locomotion is to refine and adjust the parameters of locomotion, not to establish the basic locomotor pattern. This agrees with our findings here showing heightened centrality in primary sensorimotor regions occurs during transitions to or from locomotion but is lowered once continued locomotion is reached, suggesting increased cortical communication with these regions is needed only with changes in gait. The overall decreased pattern of connectivity paired with increased activity possibly suggests that the majority of cortical regions become engaged in region-specific calculations and/or become involved in adjusting locomotion only as needed.

In contrast to M1, the role of premotor cortices in locomotion is relatively unknown (Drew and Marigold, 2015). In the mouse, M2 is implicated as essential in several discrete motor behaviors, including licking (Chen et al., 2017; Allen et al., 2017; Inagaki et al., 2018) and in a lever press task (Makino et al., 2017). Widely connected, the secondary motor areas receive inputs from the somatosensory, auditory, posterior parietal, and orbital cortices and project to primary motor, somatosensory, parietal, and retrosplenial areas (Yamawaki et al., 2016; Zhang et al., 2016; Leinweber et al., 2017; Lin et al., 2018). This widespread connectivity suggests that the premotor regions act as a link between sensory inputs, motor behavior and navigational control. In mice that learned a lever-pressing motor, M2 activity can be used to causally predict activity in other dorsal cortical regions during movement (Makino et al., 2017). Furthermore, inactivation of M2 represses cortex-wide responses to sensory stimuli (Allen et al., 2017). Together these results provide a potential neural substrate for the role of the premotor cortex in locomotion, including establishing both the observed network of increased functional connectivity involving ICs within M2 and the overall decreased connectivity pattern among other ICs.

In the primate, the premotor cortex is involved in transforming sensory information for movement planning (Di Pellegrino G. and Ladavas, 2015). Multimodal neurons in the ventral premotor cortex map visual and auditory stimuli in spatial relation to the space immediately surrounding the body, or peri-personal space (Rizzolatti et al., 1981; Graziano et al., 1994; Fogassi et al., 1996). Peri-personal space is important for both motor and cognitive computations (Serino, 2019). Inhibiting the premotor cortex impairs reaction times to stimuli in peri-personal space (Serino et al., 2011). Stimuli within peri-personal space modulate the motor system, including decreasing the excitability of M1 (Makin et al., 2009; Serino et al., 2009), and the premotor cortex is necessary for this modulation (Avenanti et al., 2012). Although primarily studied in discrete movements, these interactions between sensory and motor systems are also important in locomotion. Not only is peri-personal space utilized in locomotion, but the representation of physical distance from the body expands during walking, even when other sensory cues are stationary (Noel et al., 2015). Moreover, locomotive behavior is facilitated when salient stimuli appear far away rather than up close (Di Marco S. et al., 2019). These effects likely improve obstacle avoidance during locomotion (Noel et al., 2015) and/or promote movement toward a salient stimulus (Di Marco S. et al., 2019). Therefore, cerebral cortical involvement in locomotion includes M2 connectivity patterns in which cortical sensory, motor and navigational information is integrated into a representation of peri-personal space used to continuously plan and control motor action.

Reference List

Alexander AS, Nitz DA (2015) Retrosplenial cortex maps the conjunction of internal and external spaces. Nat Neurosci 18:1143-1151.

Allen Institute for Brain Science (2015) Technical white paper: Allen mouse common coordinate framework. Allen Institute for Brain Science 1:1-18.

Allen WE, Kauvar IV, Chen MZ, Richman EB, Yang SJ, Chan K, Gradinaru V, Deverman BE, Luo L, Deisseroth K (2017) Global representations of goal-directed behavior in distinct cell types of mouse neocortex. Neuron 94:891-907.

Avenanti A, Annela L, Serino A (2012) Suppression of premotor cortex disrupts motor coding of peripersonal space. Neuroimage 63:281-288.

Buzsaki G (2010) Neural syntax: cell assemblies, synapsembles, and readers. Neuron 68:362-385.

Calhoun VD, de LN (2017) Ten key observations on the analysis of resting-state functional MR imaging data using independent component analysis. Neuroimaging Clin N Am 27:561-579.

Cardoso JF (1999) High-order contrasts for independent component analysis. Neural Comput 11:157-192.

Carrillo-Reid L, Yang W, Bando Y, Peterka DS, Yuste R (2016) Imprinting and recalling cortical ensembles. Science 353:691-694.

Chapin JK, Woodward DJ (1982) Somatic sensory transmission to the cortex during movement: phasic modulation over the locomotor step cycle. Exp Neurol 78:670-684.

Chen TW, Li N, Daie K, Svoboda K (2017) A map of anticipatory activity in mouse motor cortex. Neuron 94:866-879.

Clancy KB, Orsolic I, Mrsic-Flogel TD (2019) Locomotion-dependent remapping of distributed cortical networks. Nat Neurosci.

Dadarlat MC, Stryker MP (2017) Locomotion enhances neural encoding of visual stimuli in mouse V1. J Neurosci 37:3764-3775.

Dana H, Chen TW, Hu A, Shields BC, Guo C, Looger LL, Kim DS, Svoboda K (2014) Thy1-GCaMP6 transgenic mice for neuronal population imaging in vivo. PLoS ONE 9:e108697.

Di Marco S., Tosoni A, Altomare EC, Ferretti G, Perrucci MG, Committeri G (2019) Walking-related locomotion is facilitated by the perception of distant targets in the extrapersonal space. Sci Rep 9:9884.

Di Pellegrino G., Ladavas E (2015) Peripersonal space in the brain. Neuropsychologia 66:126-133.

Dipasquale O, Griffanti L, Clerici M, Nemni R, Baselli G, Baglio F (2015) High-dimensional ICA analysis detects within-network functional connectivity damage of default-mode and sensory-motor networks in Alzheimer's Disease. Front Hum Neurosci 9:43.

Dipoppa M, Ranson A, Krumin M, Pachitariu M, Carandini M, Harris KD (2018) Vision and locomotion shape the interactions between neuron types in mouse visual cortex. Neuron 98:602-615.

Drew T, Andujar JE, Lajoie K, Yakovenko S (2008a) Cortical mechanisms involved in visuomotor coordination during precision walking. Brain Res Rev 57:199-211.

Drew T, Kalaska J, Krouchev N (2008b) Muscle synergies during locomotion in the cat: a model for motor cortex control. J Physiol 586:1239-1245.

Drew T, Marigold DS (2015) Taking the next step: cortical contributions to the control of locomotion. Curr Opin Neurobiol 33:25-33.

Favorov OV, Nilaweera WU, Miasnikov AA, Beloozerova IN (2015) Activity of somatosensory-responsive neurons in high subdivisions of SI cortex during locomotion. J Neurosci 35:7763-7776.

Ferezou I, Haiss F, Gentet LJ, Aronoff R, Weber B, Petersen CC (2007) Spatiotemporal dynamics of cortical sensorimotor integration in behaving mice. Neuron 56:907-923.

Fogassi L, Gallese V, Fadiga L, Luppino G, Matelli M, Rizzolatti G (1996) Coding of peripersonal space in inferior premotor cortex (area F4). J Neurophysiol 76:141-157.

Ghanbari L, Carter RE, Rynes M, Dominguez J, Chen G, Naik A, Hu J, Sagar MAK, Halton L, Mossazaghi N, Gray MM, West SL, Eliceiri KW, Ebner TJ, Kodandaramaiah SB (2019) Cortex-wide neural interfacing via transparent polymer skulls. Nature Communications 10:1500.

Ghose GM (2015) Vision and vigilance on the go. Trends Cogn Sci 19:115-116.

Godschalk M, Lemon RN, Kuypers HG, van der Steen J (1985) The involvement of monkey premotor cortex neurones in preparation of visually cued arm movements. Behav Brain Res 18:143-157.

Graziano MS, Yap GS, Gross CG (1994) Coding of visual space by premotor neurons. Science 266:1054-1057.

Greicius MD, Krasnow B, Reiss AL, Menon V (2003) Functional connectivity in the resting brain: a network analysis of the default mode hypothesis. Proc Natl Acad Sci U S A 100:253-258.

Greicius MD, Supekar K, Menon V, Dougherty RF (2009) Resting-state functional connectivity reflects structural connectivity in the default mode network. Cereb Cortex 19:72-78.

Harris KD (2005) Neural signatures of cell assembly organization. Nat Rev Neurosci 6:399-407.

Harris KD, Thiele A (2011) Cortical state and attention. Nat Rev Neurosci 12:509-523.

Inagaki HK, Inagaki M, Romani S, Svoboda K (2018) Low-dimensional and monotonic preparatory activity in mouse anterior lateral motor cortex. J Neurosci 38:4163-4185.

Jacobs EAK, Steinmetz NA, Carandini M, Harris KD (2018) Cortical state fluctuations during sensory decision making. bioRxiv 2018.

Josset N, Roussel M, Lemieux M, Lafrance-Zoubga D, Rastqar A, Bretzner F (2018) Distinct contributions of mesencephalic locomotor region nuclei to locomotor control in the freely behaving mouse. Curr Biol 28:884-901.

Kimes PK, Liu Y, Hayes DN, Marron JS (2017) "Statistical significance for hierarchical clustering". Biometrics 73:811-821.

Lee AM, Hoy JL, Bonci A, Wilbrecht L, Stryker MP, Niell CM (2014) Identification of a brainstem circuit regulating visual cortical state in parallel with locomotion. Neuron 83:455-466.

Leinweber M, Ward DR, Sobczak JM, Attinger A, Keller GB (2017) A Sensorimotor circuit in mouse cortex for visual flow predictions. Neuron 96:1204.

Liddell EGT, Phillips CG (1944) Pyramidal section in the cat. Brain 67:1-9.

Lin HM, Kuang JX, Sun P, Li N, Lv X, Zhang YH (2018) Reconstruction of intratelencephalic neurons in the mouse secondary motor cortex reveals the diverse projection patterns of single neurons. Front Neuroanat 12:86.

Ma Y, Shaik MA, Kim SH, Kozberg MG, Thibodeaux DN, Zhao HT, Yu H, Hillman EM (2016) Wide-field optical mapping of neural activity and brain haemodynamics: considerations and novel approaches. Philos Trans R Soc Lond B Biol Sci 371.

MacDowell CJ, Buschman TJ (2020) Low-dimensional spatio-temporal dynamics underlie cortex-wide neural activity. bioRxiv 2020.

Makin TR, Holmes NP, Brozzoli C, Rossetti Y, Farne A (2009) Coding of visual space during motor preparation: Approaching objects rapidly modulate corticospinal excitability in hand-centered coordinates. J Neurosci 29:11841-11851.

Makino H, Ren C, Liu H, Kim AN, Kondapaneni N, Liu X, Kuzum D, Komiyama T (2017) Transformation of cortex-wide emergent properties during motor learning. Neuron 94:880-890.

Marigold DS, Andujar JE, Lajoie K, Drew T (2011) Motor planning of locomotor adaptations on the basis of vision: The role of the posterior parietal cortex. Elsevier Progress in Brian Research 188.

McGinley MJ, David SV, McCormick DA (2015a) Cortical membrane potential signature of optimal states for sensory signal detection. Neuron 87:179-192.

McGinley MJ, Vinck M, Reimer J, Batista-Brito R, Zagha E, Cadwell CR, Tolias AS, Cardin JA, McCormick DA (2015b) Waking state: rapid variations modulate neural and behavioral responses. Neuron 87:1143-1161.

McKeown MJ, Hansen LK, Sejnowsk TJ (2003) Independent component analysis of functional MRI: what is signal and what is noise? Curr Opin Neurobiol 13:620-629.

Mohajerani MH, Chan AW, Mohsenvand M, Ledue J, Liu R, McVea DA, Boyd JD, Wang YT, Reimers M, Murphy TH (2013) Spontaneous cortical activity alternates between motifs defined by regional axonal projections. Nat Neurosci 16:1426-1435.

Musall S, Kaufman MT, Juavinett AL, Gluf S, Churchland AK (2019) Single-trial neural dynamics are dominated by richly varied movements. Nat Neurosci 22:1677-1686.

Niell CM, Stryker MP (2010) Modulation of visual responses by behavioral state in mouse visual cortex. Neuron 65:472-479.

Noel JP, Grivaz P, Marmaroli P, Lissek H, Blanke O, Serino A (2015) Full body action remapping of peripersonal space: the case of walking. Neuropsychologia 70:375-384.

Petersen TH, Willerslev-Olsen M, Conway BA, Nielsen JB (2012) The motor cortex drives the muscles during walking in human subjects. J Physiol 590:2443-2452.

Raichle ME, MacLeod AM, Snyder AZ, Powers WJ, Gusnard DA, Shulman GL (2001) A default mode of brain function. Proc Natl Acad Sci U S A 98:676-682.

Rizzolatti G, Scandolara C, Matelli M, Gentilucci M (1981) Afferent properties of periarcuate neurons in macaque monkeys. II. Visual responses. Behav Brain Res 2:147-163.

Rubinov M, Sporns O (2010) Complex network measures of brain connectivity: uses and interpretations. Neuroimage 52:1059-1069.

Sahonero-Alvarez G, Calderon H (2017) A comparison of SOBI, FastICA, JADE and infomax algorithms. IMCIC 8th International Multi-Conference on Complexity, Informatics and Cybernetics, Proceedings, 2017.

Saleem AB, Ayaz A, Jeffery KJ, Harris KD, Carandini M (2013) Integration of visual motion and locomotion in mouse visual cortex. Nat Neurosci 16:1864-1869.

Schneider DM, Mooney R (2018) How movement modulates hearing. Annu Rev Neurosci 41:553-572.

Schneider DM, Nelson A, Mooney R (2014) A synaptic and circuit basis for corollary discharge in the auditory cortex. Nature 513:189-194.

Serino A (2019) Peripersonal space (PPS) as a multisensory interface between the individual and the environment, defining the space of the self. Neurosci Biobehav Rev 99:138-159.

Serino A, Annella L, Avenanti A (2009) Motor properties of peripersonal space in humans. PLoS ONE 4:e6582.

Serino A, Canzoneri E, Avenanti A (2011) Fronto-parietal areas necessary for a multisensory representation of peripersonal space in humans: an rTMS study. J Cogn Neurosci 23:2956-2967.

Sharma S, Kim LH, Whelan PJ (2019) Towards a connectome of descending commands controlling locomotion. Science Direct (Elsevier) Current Opinion in Physiology.

Shimaoka D, Harris KD, Carandini M (2018) Effects of arousal on mouse sensory cortex depend on modality. Cell Rep 22:3160-3167.

Takakusaki K (2017) Functional neuroanatomy for posture and gait control. J Mov Disord 10:1-17.

Vanni MP, Chan AW, Balbi M, Silasi G, Murphy TH (2017) Mesoscale mapping of mouse cortex reveals frequency-dependent cycling between distinct macroscale functional modules. J Neurosci 37:7513-7533.

Vanni MP, Murphy TH (2014) Mesoscale transcranial spontaneous activity mapping in GCaMP3 transgenic mice reveals extensive reciprocal connections between areas of somatomotor cortex. J Neurosci 34:15931-15946.

Xiao D, Vanni MP, Mitelut CC, Chan AW, LeDue JM, Xie Y, Chen AC, Swindale NV, Murphy TH (2017) Mapping cortical mesoscopic networks of single spiking cortical or sub-cortical neurons. Elife 6.

Yamawaki N, Radulovic J, Shepherd GM (2016) A corticocortical circuit directly links retrosplenial cortex to M2 in the mouse. J Neurosci 36:9365-9374.

Zhang S, Xu M, Chang WC, Ma C, Hoang Do JP, Jeong D, Lei T, Fan JL, Dan Y (2016) Organization of long-range inputs and outputs of frontal cortex for top-down control. Nat Neurosci 19:1733-1742.

Zhou M, Liang F, Xiong XR, Li L, Li H, Xiao Z, Tao HW, Zhang LI (2014) Scaling down of balanced excitation and inhibition by active behavioral states in auditory cortex. Nat Neurosci 17:841-850.

Figures and Legends

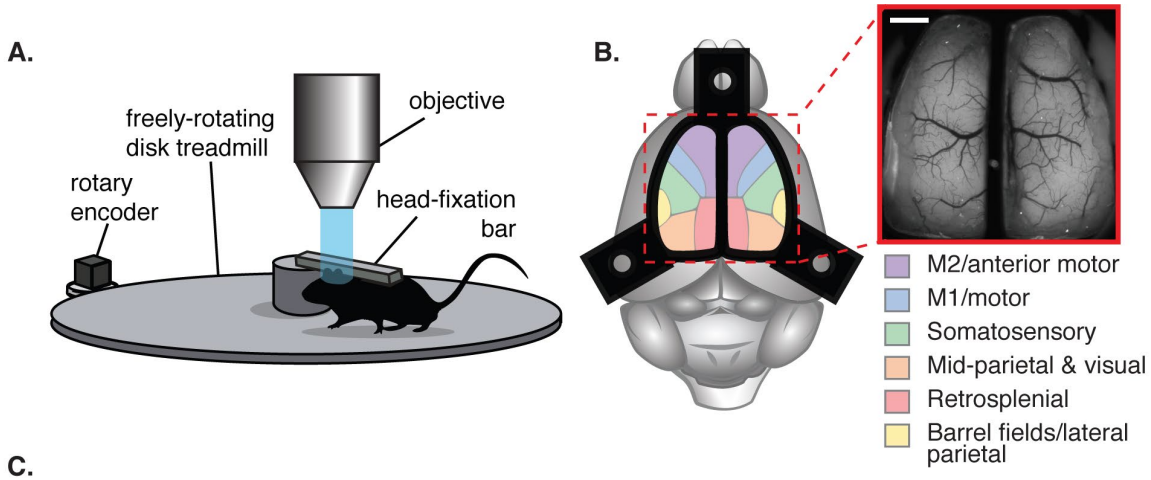

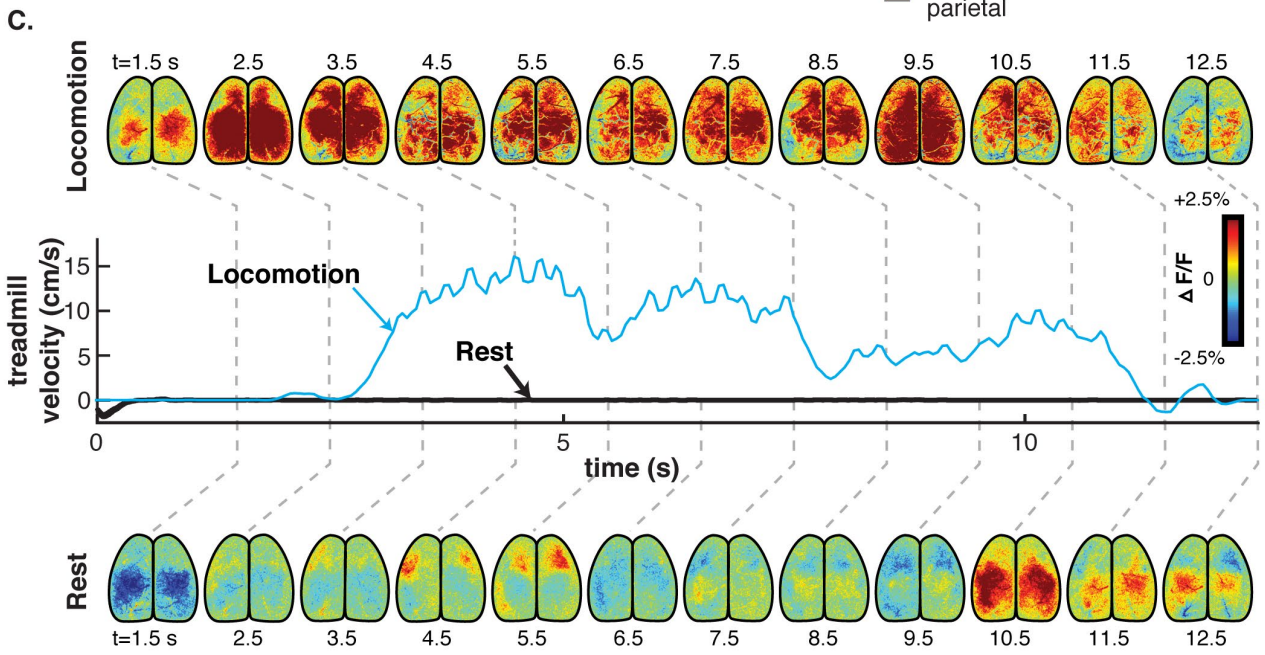

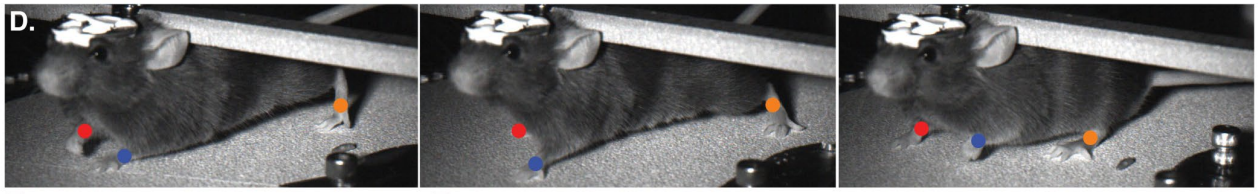

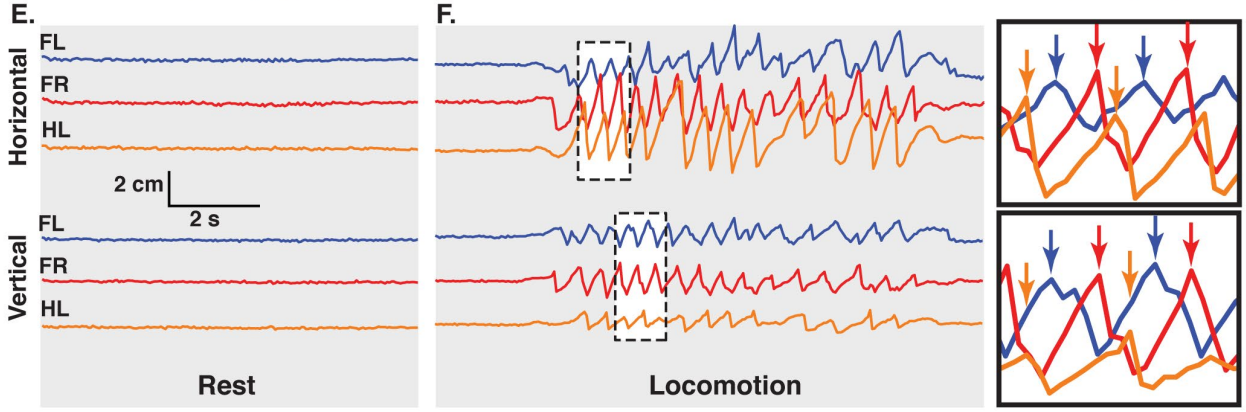

Figure 1. Mesoscopic cortical recording set up and activity during locomotion. **A.** Experimental set-up for behavioral and Ca^{2+} fluorescence imaging of head fixed mice. **B.** Approximate cortical regions, as defined by the Allen Brain Atlas Common Coordinate Framework (Allen Institute for Brain Science, 2015), observable through the polymer skull (inset) by epifluorescence microscopy. Scale bar = 1 mm. Common Framework colors correspond to cortical regions defined in key. **C.** Treadmill velocity (middle) is plotted for two example behavior periods in a single mouse: rest (thick black line) and locomotion (blue line) activity. Grey dashed lines link plots of cortical Ca^{2+} fluorescence during each time point during rest (bottom) and locomotion (top). Cortical activity shown as a % change in fluorescence ($\Delta F/F$) compared to rest. For visualization only, frames were spatially filtered with a 3x3 moving mean and averaged across 5 frames. **D.** Manual tracking of paw positions for example periods of rest and locomotion. Blue, front left paw (FL); red, front right paw (FR); orange, hind left paw (HL). **E.** Horizontal (top) and vertical (bottom) paw displacements vs. time during rest and **F.** During locomotion. Maximum displacement of each paw (inset, arrows) show stereotypic, repeating step cycle.

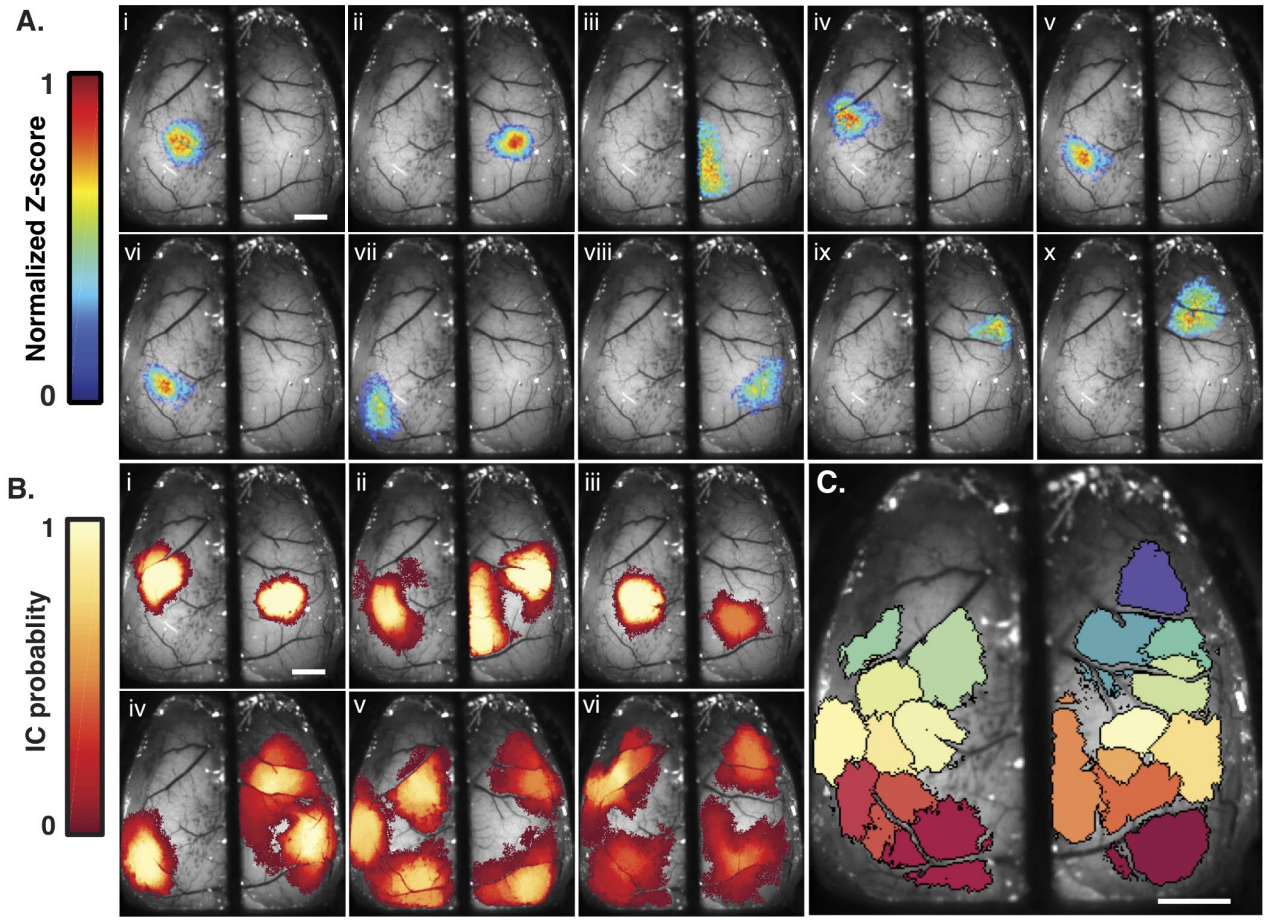

Figure 2. Functional segmentation of cerebral cortical activity for individual recording sessions. **A.** Spatial ICs calculated from an example one-minute time segment of Ca^{2+} imaging. **B.** Overlay of the z-score maps of the IC clusters from example session shows consistency of ICs within a recording day. **C.** Example masks of the IC clusters from one recording session. For visualization, masks are created from the combined IC z-score maps of the clusters thresholded at 0.3 x the maximum z-score. ICs are colored for visualization based on the anterior-posterior location of the IC's center of mass.

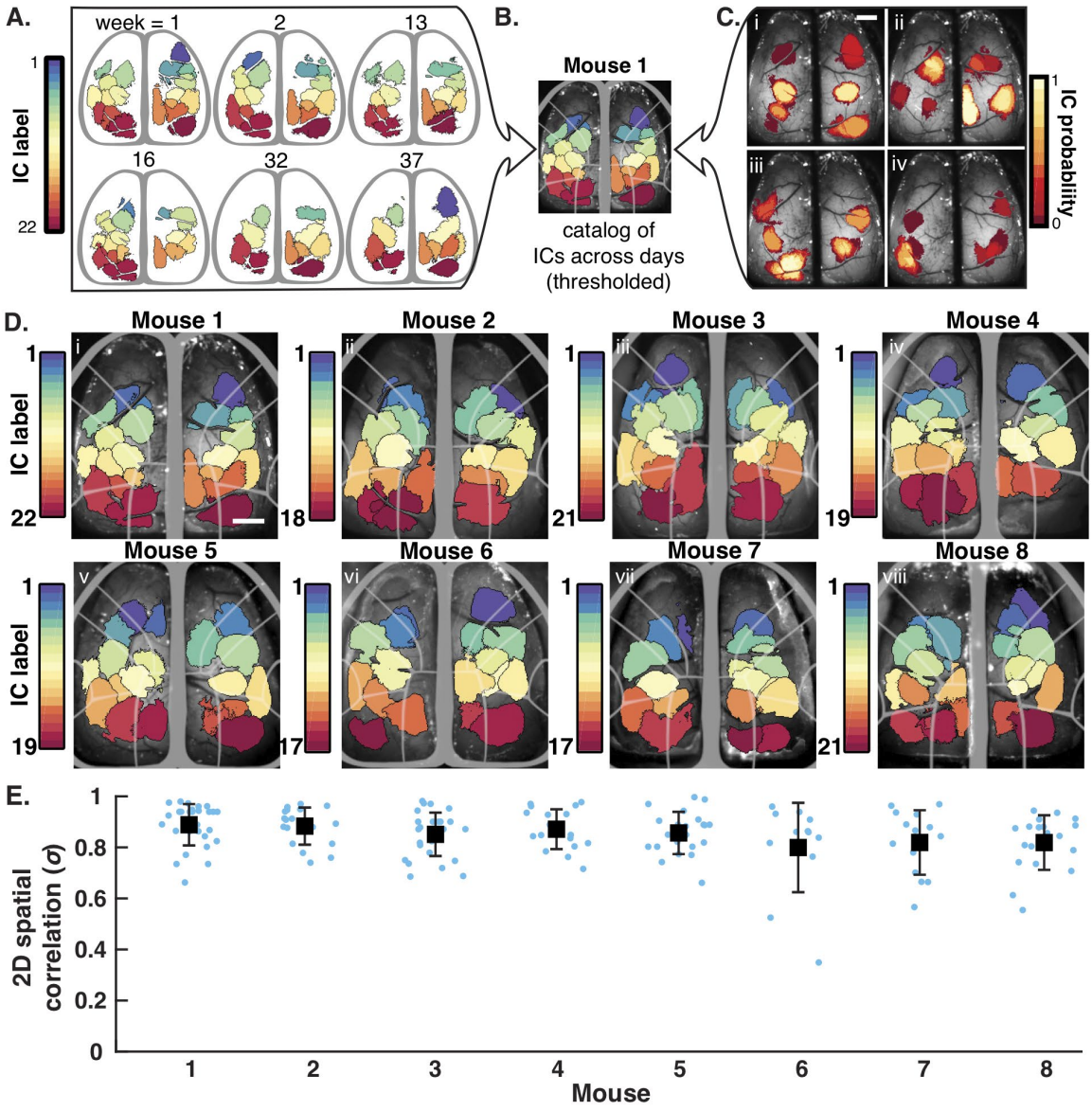

Figure 3. IC catalogs generated from Ca^{2+} imaging data for each animal. **A.** Significant IC clusters in a single mouse, calculated from 6 example recording days, each collected over a multi-week time period. Masks of IC clusters are plotted as in Figure 2. Reoccurring clusters are labeled in the same color. **B.** Overlaid masks of reoccurring IC clusters across all recording sessions of Mouse 1. **C.** To generate an IC catalog for each mouse, reoccurring IC clusters identified in (A) and (B) are grouped, and their z-score maps are averaged and thresholded (> 0.3 of maximum z-score). Scale bar = 1mm. **D.** IC catalogs by individual mouse. Catalog ICs are colored for visualization based on the anterior-posterior location of the catalog IC's center of mass. **E.** Distribution (mean ± s.d.) of the mean spatial correlation of significant recurring clusters across recording sessions. Blue dots correspond to the mean spatial correlation for a single IC within a cluster across sessions. Number of blue dots represent number of clusters in each the catalog from each animal.

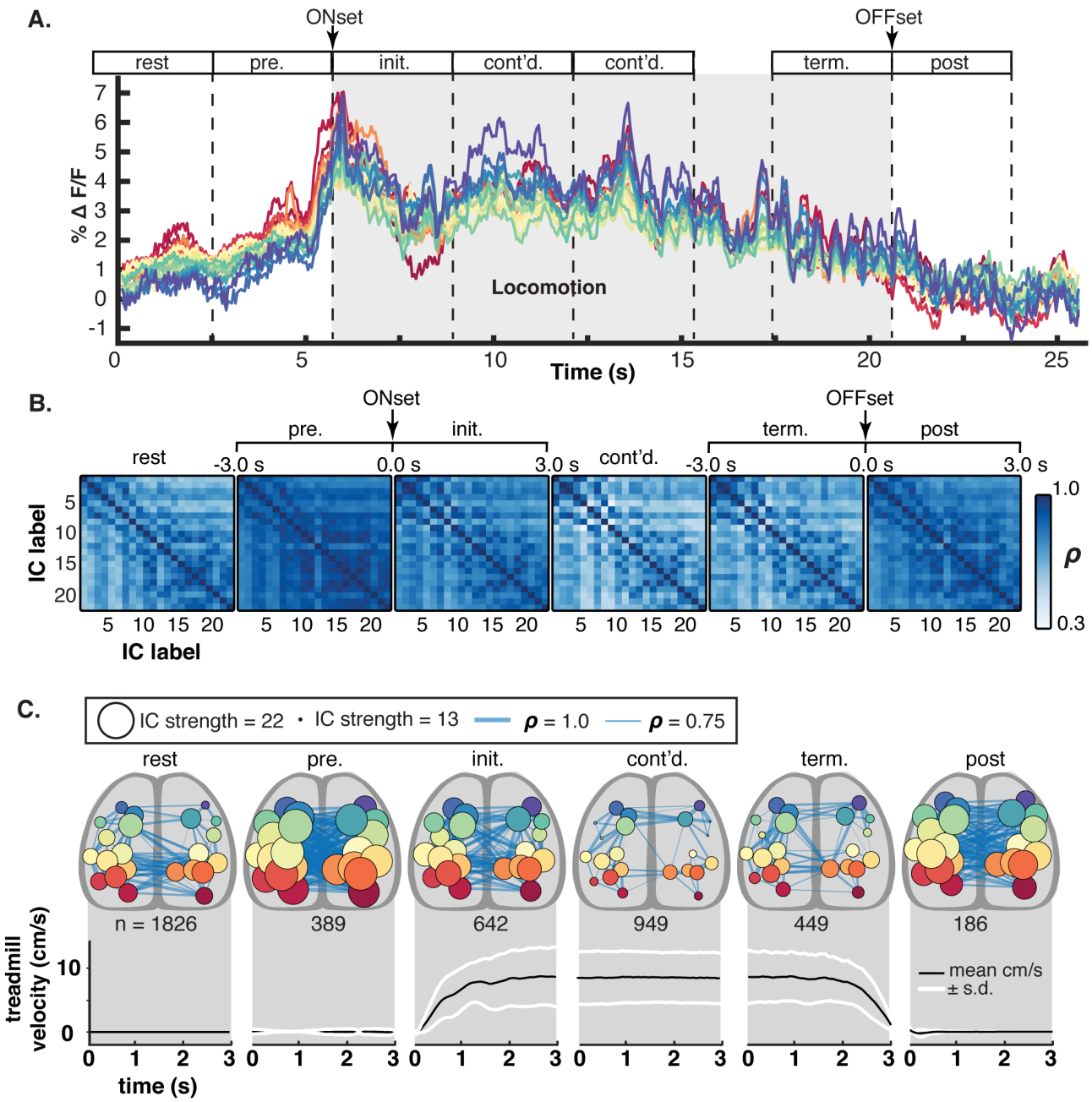

Figure 4. Changes in functional connectivity among cortical ICs during transitions rest to walk and walk to rest across in a single mouse. **A.** Fluorescence time series extracted from the catalog ICs (colored lines correspond to the ICs shown in Figure 3D.i) from rest to locomotion and return. ΔF/F was calculated as the % change in fluorescence from the mean fluorescence of the rest period preceding the locomotion period. All data are from Mouse 1. Abbreviations: pre., pre-locomotion; init., initiation of locomotion; cont'd., continued locomotion; term., termination of locomotion; post, post-locomotion. **B.** Correlation matrices for the catalog ICs for each period. Correlation coefficients (ρ) are the average from all 3s periods for each period. **C.** Top: Network graph representation of correlations shown in (B). Circles (nodes) depict each IC, while connecting lines (edges) depict $\rho > 0.75$. The size of a node indicates the strength (summed correlations) of an IC. n = number of 3s time periods included in each behavior period. Bottom: Mean (black lines) and standard deviation (s.d.,white lines) of treadmill velocity across each behavioral time period. ICs are colored for visualization based on the anterior-posterior location of the IC's center of mass.

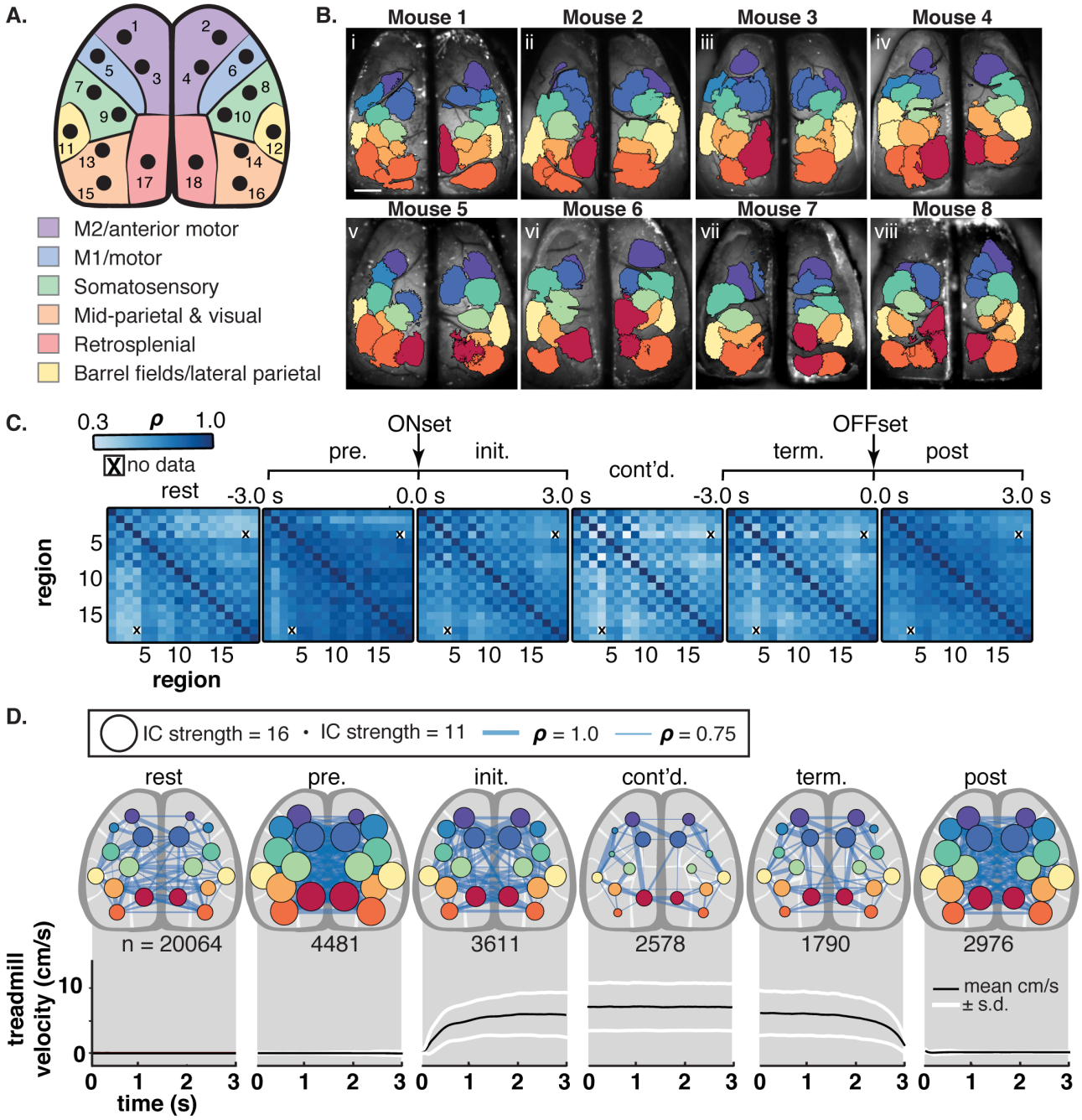

Figure 5. Changes in functional connectivity among cortical ICs during behavior transitions across all mice. **A.** Diagram of functional regions found to be consistently represented by catalog ICs across mice mapped onto the Common Coordinate Framework (Allen Institute for Brain Science, 2015). Region color correspond to key in Fig. 1B. **B.** Functional regions that occur by individual IC catalog. Colors correspond to diagram in A. Scale bar = 1 mm. **C.** Averaged correlation matrices for ICs located across all mice. X denote the lack of correlations between ICs 4 and 17, which never occurred in the same mouse. **D.** Top: Graphical representation of the correlations shown in (B), similar to that in Figure 4 (C). Connecting edges indicate $\rho > 0.75$. n = number of 3s time periods included in each behavior period. Bottom: Mean (black lines) and s.d. (white lines) of treadmill velocity across each behavioral time period for all mice. IC colors correspond to Common Coordinate Framework coded in A. ICs of the same hue, but different intensities, represent different ICs located in the same atlas region.

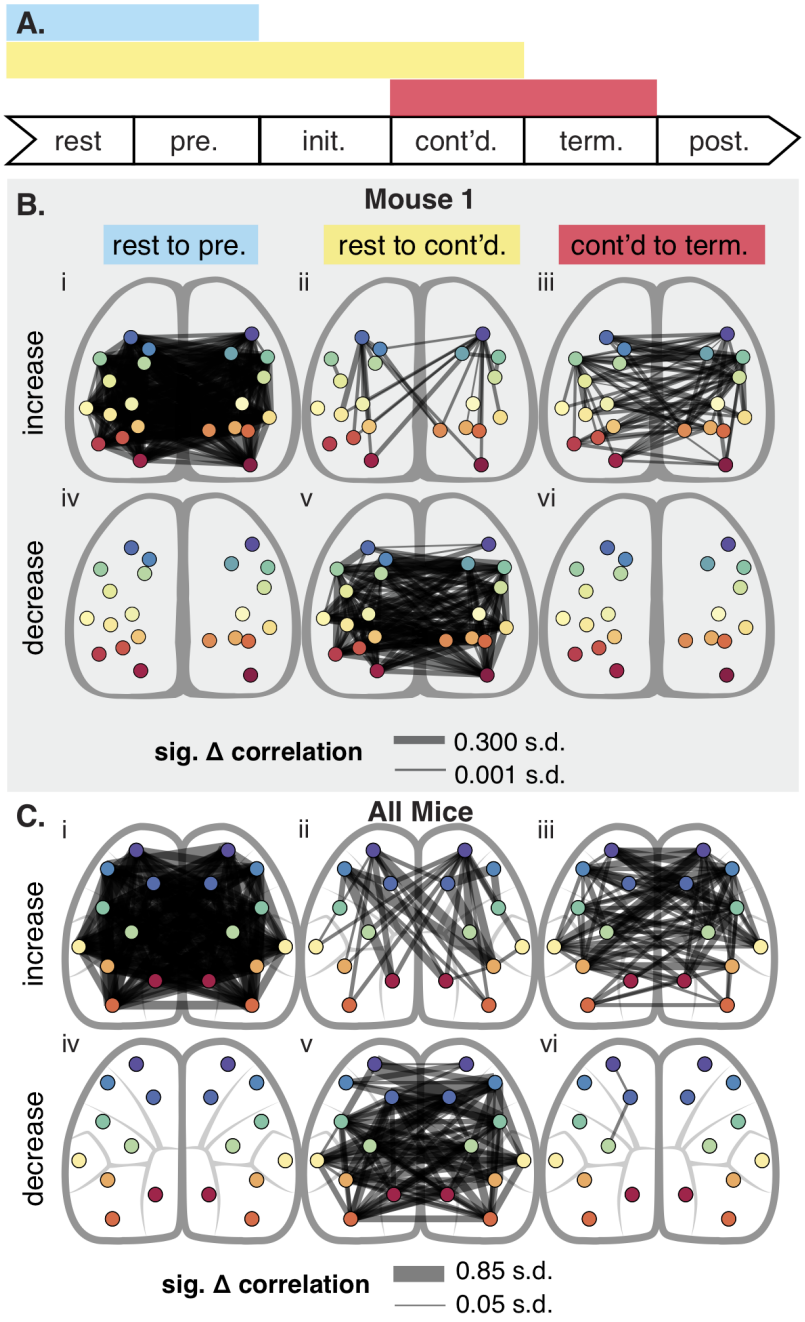

Figure 6. Significant changes in correlations between IC regions across behavioral periods. **A.** Behavioral time periods compared in (B) and (C). **B.** Significant increases (top) and decreases (bottom) in IC correlation across behavior periods in a single mouse. ($\alpha<0.05$, permutation distribution of t-statistics with Bonferroni correction). As correlations were normalized across recording days, the magnitude of the change is expressed in standard deviations from the mean of all correlations used. ICs are colored for visualization based on the anterior-posterior location of the IC's center of mass. **C.** Significant increases (top) and decreases (bottom) in normalized correlation across a subset of behavior periods in all mice ($\alpha<0.05$, permutation distribution of t-statistics with Bonferroni correction). Layout of behavioral time period comparisons same as in (B). As in (B), the magnitude of the change is expressed in standard deviations from the mean of all correlations used. IC colors correspond to Common Coordinate Framework coded in Fig 5A. ICs of the same hue, but different intensities, represent different ICs located in the same atlas region.

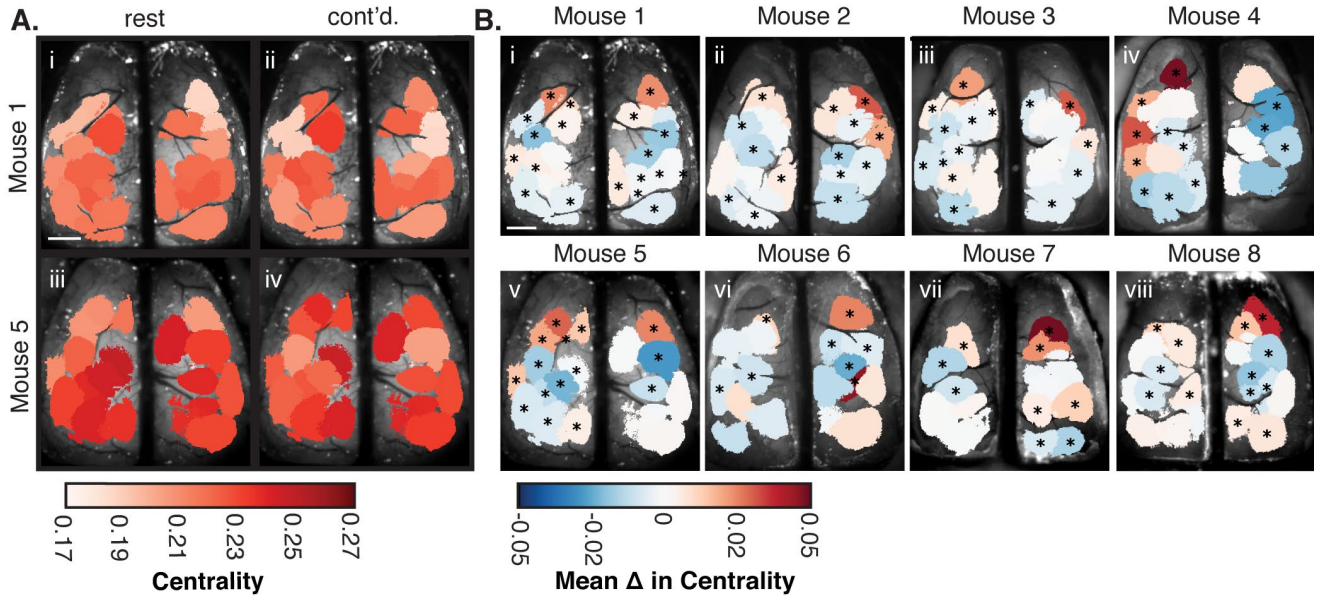

Figure 7. Eigenvector centrality of ICs in individual mice. **A.** Mean eigenvector centrality of ICs during rest (left) and continued locomotion (right) in 2 example mice (top and bottom). **B.** Mean change in eigenvector centrality from rest to continued locomotion for each animal used in the study. * indicates a significant change ($\alpha < 0.05$, permutation distribution of t-statistics with Bonferroni correction). Scale bars = 1mm.

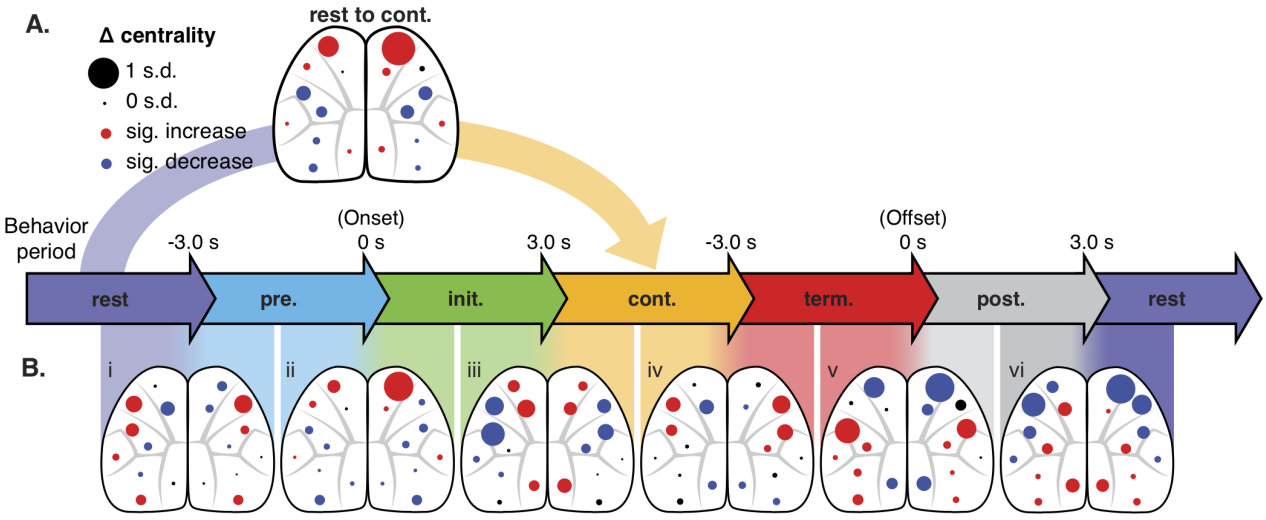

Figure 8. Summary of significant changes in normalized centrality across transitions of adjacent behavior periods for all mice. **A.** Significant change in normalized centrality from rest to continued locomotion across all mice. Size of circles indicate magnitude of the change, while circle color represents direction of significant change (red=increase, blue=decrease, black=not significant; $\alpha<0.05$, permutation distribution of t-statistics with Bonferroni correction). Block arrows represent 3s behavior periods of locomotion time course analyzed in this study (as in Fig. 6A). Colored background shading represents transition time period over which change in centrality was calculated. **B.** Significant change in normalized centrality across sequential behavior periods. Colored background shading connects transition time course used to calculate centrality between each behavior period with the corresponding plot (i-vi). Color and size of circles are the same as in (A).

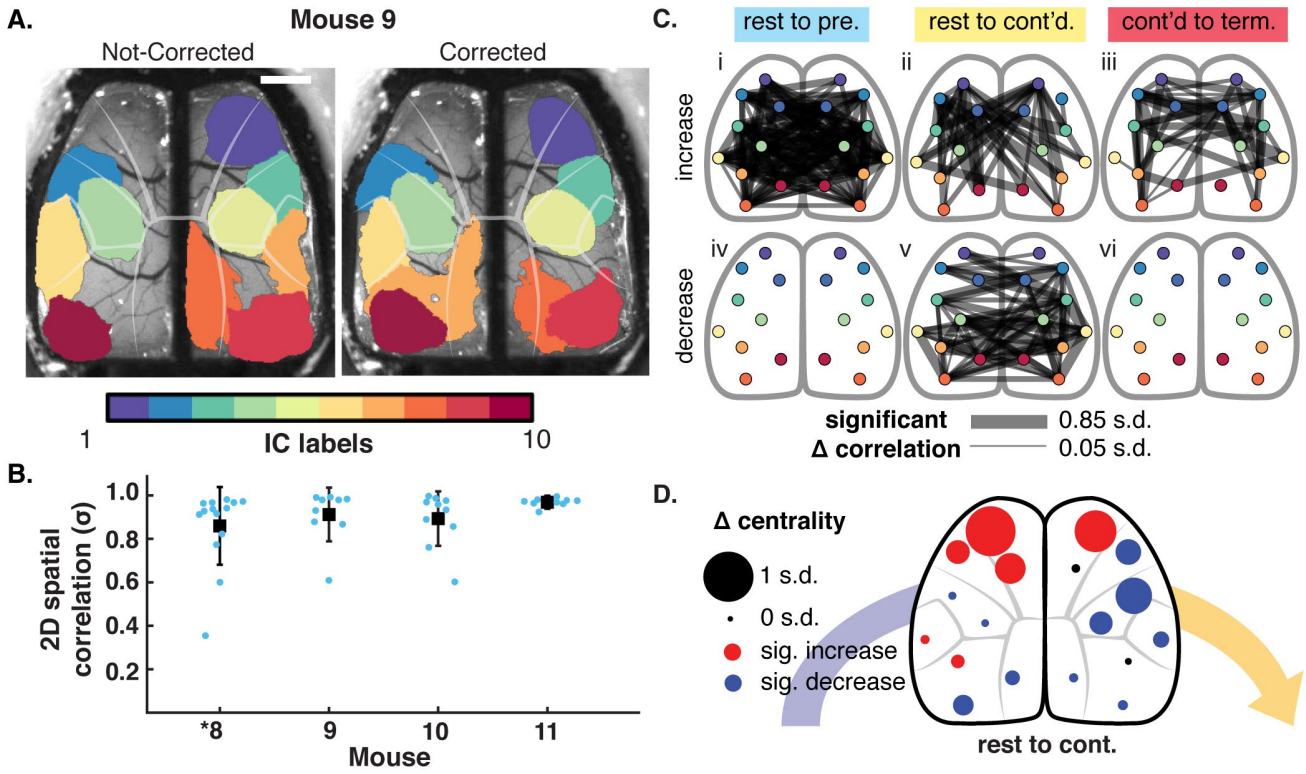

Figure 9. Results of hemodynamic corrected imaging data with ICA methods. **A.** IC catalog generated from not-corrected (left) and corrected (right) data from a single mouse. Scale bar = 1 mm, for both images. ICs are colored for visualization based on the anterior-posterior location of the IC's center of mass. **B.** In each mouse, 2D spatial correlations of catalog ICs generated from not-corrected imaging data to the corresponding catalog IC generated from the hemodynamic corrected data. * denotes mouse used for both hemodynamic correction experiments as well as main analyses in the paper. IC colors correspond to Common Coordinate Framework coded in Fig 5A. ICs of the same hue, but different intensities, represent different ICs located in the same atlas region. **C.** Significant increases (top) and decreases (bottom) in normalized correlation across a subset of behavior periods in all hemodynamic corrected mice, similar to Fig. 6C ($\alpha < 0.05$, permutation distribution of t-statistics with Bonferroni correction). **D.** Significant change in normalized centrality from rest to continued locomotion across all hemodynamic corrected mice. Size of circles indicate magnitude of the change, while circle color represents direction of significant change, as in Fig. 8A.